Extended Conjugation Refining Carbon Nitride for Non-sacrificial H_2O_2 Photosynthesis and Hypoxic Tumor Therapy

Jin Ma,[a] Xiaoxiao Peng,[a] Zhixin Zhou,[a] Hong Yang,[a] Kaiqing Wu,[a] Zhengzou Fang,[b] Dan Han,[a] Yanfeng Fang,[a] Songqin Liu,[a] Yanfei Shen,[b] Yuanjian Zhang[a]*

[a]Jiangsu Engineering Laboratory of Smart Carbon-Rich Materials and Device, Jiangsu Province Hi-Tech Key Laboratory for Bio-Medical Research, School of Chemistry and Chemical Engineering, Southeast University, Nanjing 211189, China, E-mail: Yuanjian.Zhang@seu.edu.cn

[b]Medical School, Southeast University, Nanjing 210009, China

Abstract

Artificial photocatalysis offers a clean approach for producing H_2O_2. However, the poor selectivity and activity of H_2O_2 production hamper traditional industrial applications and emerging photodynamic therapy (PDT)/chemodynamic therapy (CDT). Here, we report a well-defined C_5N_2 photocatalyst with a conjugated C=N linkage for highly selective and efficient non-sacrificial H_2O_2 production both in normoxic and hypoxic systems. The strengthened delocalization of π–electrons by linkers in C_5N_2 significantly downshifted the band position, which eliminated the side photoreduction reaction of H_2 evolution in thermodynamics and promoted water oxidation ability in kinetics. As a result, C_5N_2 had a competitive overall H_2O_2 production with solar-to-chemical conversion efficiency of 0.55% and more interestingly, exhibited the highest activity so far in hypoxic condition (698 μM/h). C_5N_2 was further applied to hypoxic PDT/CDT, exhibiting outstanding performance in conspicuous cancer cell death and synchronous bioimaging. It shed light on unlocking linker functions in electronic structure engineering of carbon nitrides for highly efficient overall photosynthesis of H_2O_2 and expanded the scope of their prospective application in health care.

Keywords: photocatalysis, carbon nitrides, hydrogen peroxide, electron delocalization, hypoxic tumor

Introduction

Hydrogen peroxide (H_2O_2) has drawn increasing attention due to its strong oxidization power, environmentally friendly nature, and high energy density,[1] making it suitable for various applications such as clean fuels, wastewater treatment, disinfection, cleaning, and organic synthesis.[2] As a natural metabolite of many organisms, H_2O_2 has also been widely used in biomedicine, including sensing and cancer therapy, due to its endogenous nature.[3] For instance, decomposition of H_2O_2 can alleviate O_2 deficiency in the hypoxic tumor microenvironment, thereby enhancing the efficacy of photodynamic therapy (PDT).[4] Moreover, H_2O_2 can be catalyzed to generate highly reactive hydroxyl radicals (•OH) via the Fenton reaction in chemodynamic therapy (CDT).[5] Nonetheless, H_2O_2 is primarily manufactured by the anthraquinone method, which is high energy-consuming and environmentally unfriendly.[6] Thus, developing an efficient, economic, and clean approach for H_2O_2 synthesis is imperative.

$O_2 + 2H^+ + 2e^- \rightarrow H_2O_2$	0.69 V vs. NHE	(1)
$2H_2O + 4h^+ \rightarrow O_2 + 4H^+$	1.23 V vs. NHE	(2)
$2H_2O + 2h^+ \rightarrow H_2O_2 + 2H^+$	1.76 V vs. NHE	(3)
$2H^+ + 2e^- \rightarrow H_2$	0 V vs. NHE	(4)
$O_2 + 4H^+ + 4e^- \rightarrow 2H_2O$	1.23 V vs. NHE	(5)

Recent efforts demonstrated that semiconductor-based photocatalysts, particularly without any sacrificial agents, hold great potential in H_2O_2 production due to their safe, environmentally friendly, and sustainable processes.[7] In principle, for non-sacrificial H_2O_2 photosynthesis, both highly selective $2e^-$ O_2 reduction reaction (ORR) and $2e^-/4e^-$ water oxidation reaction (WOR) are needed (Eq. 1-3).[8] Nonetheless, due to the mismatching between band position of photocatalysts and standard electrode potential of the above reactions along with the overpotential, the side reactions, such as hydrogen evolution reaction (HER) and $4e^-$ ORR (Eq. 4-5) would also occur substantially.[9] Among various solutions, metal-free polymeric semiconductors, such as polymeric carbon nitrides have attracted substantial attention.[10] It was because the rich active sites of imine (C=N) in repetitive triazine/heptazine units would receive photogenerated electrons for $2e^-$ ORR, while the adjustable marginal sites could capture the photogenerated holes for water oxidation reaction (WOR).[11] To further improve non-sacrificial ORR and WOR efficiency for H_2O_2 photosynthesis, plenty of ingenious strategies in electronic structures engineering have emerged, such as

heteroatom doping (e.g., P or Sb),[12] surface defect engineering (e.g., C≡N groups and N vacancies),[11b] construction of heterojunction (e.g. C_3N_4/ pyromellitic diimide),[10a, 13] and modulating triazine/heptazine based frameworks (e.g., by spatially separated redox centers).[2d, 11a, 14] For practical applications, H_2O_2 photosynthesis still suffers, however, from low selectivity and activity, e.g., (1) most carbon nitrides could not exclude side HER reaction in thermodynamics, which not only reduces H_2O_2 photosynthesis efficiency but also poses safety risks for large-scale production; (2) the efficiency of current state-of-the-art photocatalysts for non-sacrificial H_2O_2 generation under hypoxic environment are essentially low, thus greatly limiting PDT/CDT application owing to key feature of the tumor microenvironment ($pO_2 \leqslant 5$ mmHg). Therefore, discovery of highly efficient and selective metal-free photocatalysts for non-sacrificial H_2O_2 production, particularly workable in hypoxic conditions, is a grand challenge.

Herein, we report the synthesis of well-defined C_5N_2 with a conjugated C=N linkage via Schiff base reaction to address the above restrictions in photosynthesis of H_2O_2. Due to the strengthened delocalization of π-electrons, C_5N_2 showed unusually low conduction (> 0 V vs. NHE) and valence band position, promoting a realistic selectivity of in thermodynamics and high activity in kinetics for overall H_2O_2 production via synergistic $2e^-$ ORR and $2/4e^-$ WOR. As a result, C_5N_2 rivaled the state-of-the-art photocatalysts without sacrificial reagents and co-catalysts for H_2O_2 production, [[12a], [2d], [8] [11a, 14]] and exhibited the best activity in hypoxic conditions among metal-free polymers to our knowledge. Based on this, C_5N_2 was successfully applied to hypoxic tumor PDT/CDT for the first time, demonstrating competitive performances. This work would open a new avenue for highly efficient and selective photosynthesis of H_2O_2, particularly in hypoxic conditions, and advance their intriguing applications from energy, environments, and chemical synthesis to health.

Results and discussion

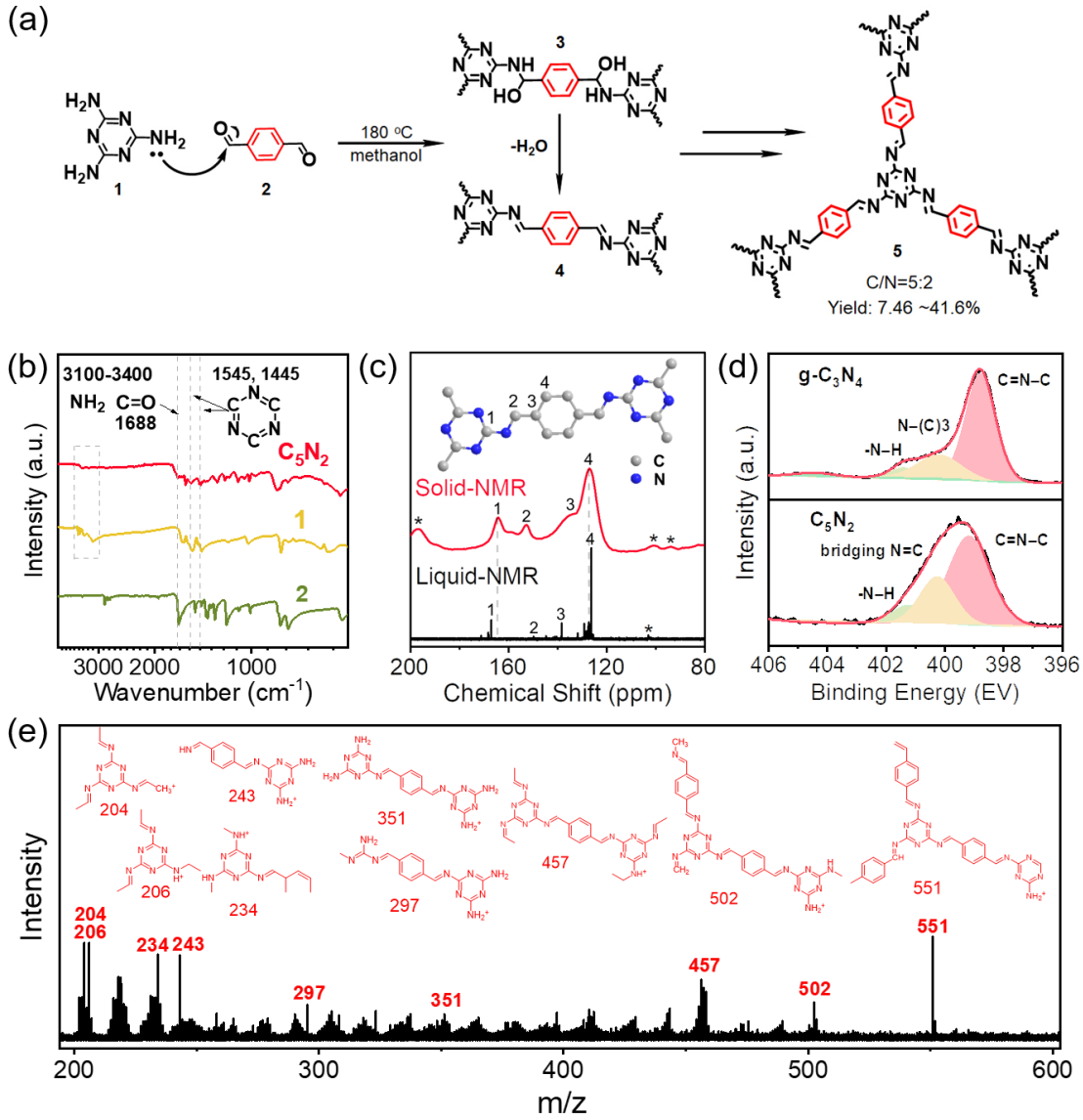

Figure 1. (a) Scheme of conjugated linker formation in the synthesis of C_5N_2 (**5**) from melamine (**1**) and p-phthalaldehdye (**2**) via Schiff base reactions. (b) FT-IR spectra of C_5N_2, **1**, and **2**. (c) Solid-state ^{13}C NMR spectra of the insoluble part and liquid-state ^{13}C NMR spectra of the dissoluble part of C_5N_2. (d) High-resolution N_{1s} XPS spectra of C_5N_2 and traditional g-C_3N_4. (e) LDI mass spectrum of C_5N_2 and their possible assignments.

Fig. 1a illustrates the general principle of the synthesis of C_5N_2 (**5**), using melamine (**1**) and p-phthalaldehdye (**2**) as the monomers in an idealized molar ratio of 3:2 via the Schiff base reaction with the intermediate product **3** and **4**.[15] To understand the reaction kinetics, the influence of reaction time on C_5N_2 formation was explored. It was found that the yield of insoluble solid products gradually increased with the increase of the

reaction time and reached a plateau after 5 days (**Table S1**). Moreover, superacid catalysts (e.g., $Sc(OTf)_3$) could accelerate the formation and exchange of double-bond linkage between aromatic aldehydes and primary amines, thus improving the yield up to 3 times.[16] From the FT-IR spectra of the solid products collected at different time intervals (Fig. S1), the relative intensity of characteristic vibration peaks of NH_2 (3100-3500 cm^{-1}) and C=O (1688 cm^{-1}) groups gradually weakened, and almost disappeared in the final C_5N_2 (Fig. 1b). The peaks at 1545 cm^{-1} and 1445 cm^{-1}, assigned to characteristic vibrations of the aromatic C=N heterocycles and imine (C=N) linkage, were observed in C_5N_2 (Fig. 1b), indicating the stepwise consuming of the monomers and the retention of the triazine unit during Schiff base polymerization reaction.[17] The combustion elemental analysis showed that the C/N molar ratio gradually increased with the longer reaction times and reached a plateau (**Table S2**) of 2.52. It was very close to the theoretical value of 2.5, suggesting the successful Schiff base reaction for C_5N_2 synthesis (Fig. 1a).[18]

The solid-state ^{13}C NMR spectrum of C_5N_2 (Fig. 1c) further confirmed the successful synthesis of C_5N_2. The C (1) atoms in triazine units at 164.5 ppm, generally, were observed at lower chemical shifts due to the strengthened delocalization of π−electrons by imine in compared to that of **1** (Fig. S2). The peaks at 136.3 and 127.2 ppm verified the C (3) and C (4) atoms in the resolved resonances for peripheral phenyl ring units, respectively, almost identical to **2**. Moreover, the disappearance of the peak at 193.5 ppm in ^{13}C spectrum and the peak at 10.1 ppm in ^{1}H of **2** in C_5N_2 (Fig. 1c and S2) were noted, indicating the complete depletion of the aldehyde carbonyl in **2**.[19] In addition, some C_5N_2 oligomer was also found in the decanted supernatant after careful separation and purification. Thanks to good solubility in methanol-d4, the liquid-state ^{13}C NMR spectrum gave peaks with a much narrower full width at half maximum (FDHM), indicative of a higher resolution compared with the solid-state one (Fig. 1c).[20] The sharp peaks with chemical shifts at 126.0 and 138.4 ppm can be more readily assigned to the phenyl ring C (4) and C (3) atoms. And, the peaks at 167.1 and 150.1 ppm were ascribed to the C (1) atom signals from the triazine ring and C (2) atom signals of the conjugated imine linkage (C=N), further validating the analysis of the solid-state NMR data.

More information on the chemical structure of C_5N_2 was obtained by X-ray photoelectron spectrum (XPS) and laser desorption/ionization (LDI) mass spectrum. Fig. 1d showed the high-resolution N_{1s} XPS spectra of traditional g-C_3N_4 and C_5N_2.

Due to the formation of the bridging N=C bond, the N_{1s} XPS peak positions of C_5N_2 were altered from those in g-C_3N_4; namely, the peak at 400.9 eV can be ascribed to the bridging N=C, and the peak for the C=N-C bonding shifted to 399.2 eV. High-resolution C_{1s} XPS spectra (Fig. S3) also revealed similar information. [21] Consistently, the laser desorption/ionization mass spectrum (LDI-MS) of C_5N_2 in Fig. 1e demonstrated m/z peaks attributable to the ablation products of the repetitive imidazole units of different link manners in C_5N_2.[22] Therefore, the proposed C_5N_2 with conjugated linkage was successfully synthesized by Schiff base reaction.

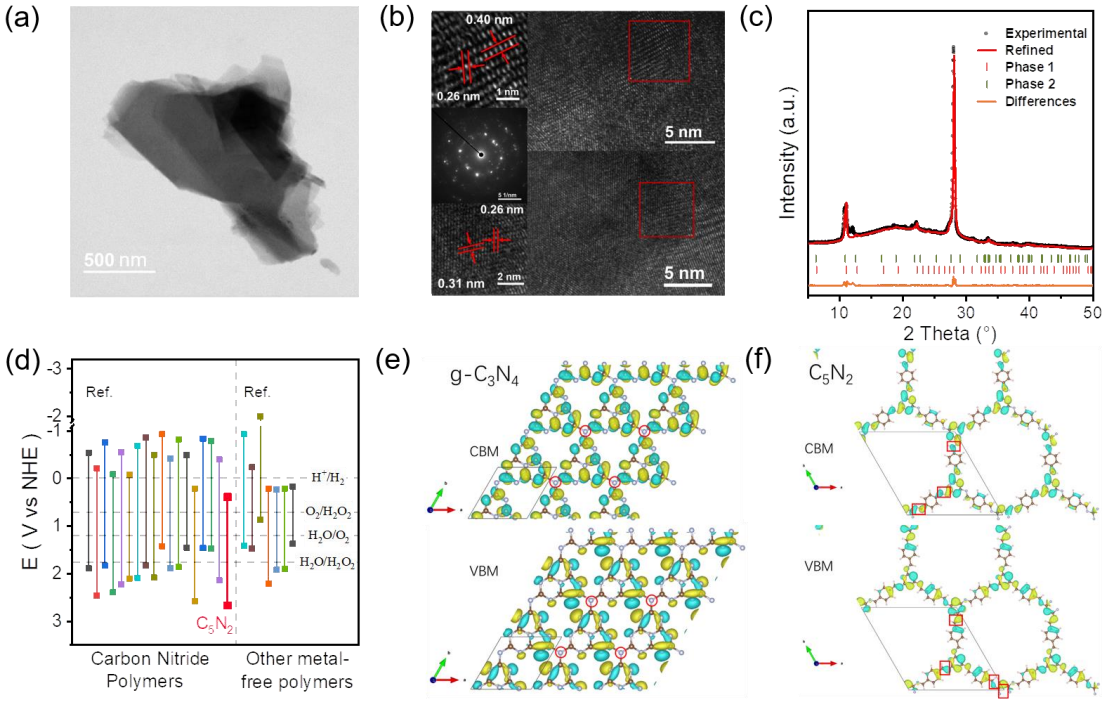

Figure 2. (a) TEM and (b) HAADF-STEM and fast Fourier transform (FFT) image of C_5N_2. Inset: enlarged HR-TEM images from the red square marked area. (c) Experimental and Pawley-refined PXRD patterns of C_5N_2. (d) CB/VB position of C_5N_2 and other reported metal-free photocatalysts.[2a, c, d, 10-11, 12b, 13-14, 23] Simulated HOMO-LUMO electronic structure distribution of (e) g-C_3N_4 and (f) C_5N_2 by DFT calculations.

The morphology of the C_5N_2 was studied with transmission electron microscopy (TEM), which demonstrated a layered texture with a lateral size over a few hundred nanometers (Fig. 2a). The high-angle annular dark-field scanning TEM (HAADF-STEM) image (Fig. 2b) and the fast Fourier transform (FFT) image of the C_5N_2 revealed a locally ordered highly crystalline characteristic. The lattice fringes with a spacing of 0.31 nm corresponded to the (002) plane, consistent with the facet in the X-ray

diffraction (XRD) pattern (Fig. 2c). The XRD pattern further disclosed minor peaks at 2θ values of 22.1° and 33.4°, which matched well with other lattice fringes in the high-resolution TEM image. Besides, the Pawley refinement plot provided good agreement factors for the experimental XRD data.[24] The high crystallinity, associated with average surface area (10.717 m^2 g^{-1}, Fig. S4), indicated the high efficiency of Schiff base reaction in synthesis of condensed carbon nitride frameworks.

Owing to the strengthened delocalization of π–electrons by linkers, the electronic band structures of C_5N_2 were supposed to change remarkably. The UV-Vis spectra of C_5N_2 with different polymerization degrees showed a characteristic broad absorption band with a distinctive absorption edge for semiconductors (Fig. S5). The absorption edge gradually increased from 515 to 544 nm, corresponding to the bandgap from 2.42 to 2.28 eV, with the increase of the polymerization time. Compared with g-C_3N_4 whose absorption edge was at ca. 447 nm, the absorption edge of C_5N_2 red-shifted by 97 nm. Likewise, the maximum fluorescent emission wavelength of C_5N_2 red-shifted over that of g-C_3N_4 by 90 nm (Fig. S6). To further estimate the conduction band (CB) and valence band (VB) position of C_5N_2, XPS VB scan of C_5N_2 and g-C_3N_4 (Fig. S7) and E_{fb} of g-C_3N_4 (Fig. S8) were recorded and compared.[25] Interestingly, a significant downshift of the CB and VB position of C_5N_2 with respect to conventional g-C_3N_4 and other metal-free polymers, was noted (Fig. 2d, S9). The CB of C_5N_2 was even exceptionally lower than 0 V vs NHE, which was highly envisioned to drive a highly selective O_2 reduction into H_2O_2 without competitive HER in thermodynamics; meanwhile the lower CB would lead to a stronger WOR in kinetics.

The DFT calculation of g-C_3N_4 and C_5N_2 was explored to get molecular insights into the significantly altered electronic structure (Fig. S10, S11). As nodes, Fig. 2e showed the tertiary N linkage in g-C_3N_4 broke the conjugation over the heptazine rings, which restricted the electrons to be fully delocalized in the HOMO/LUMO orbitals. In contrast, the charge density in the conjugated linkers was redistributed in C_5N_2 units, resulting in the strengthened delocalization of π–electrons (Fig. 2f). Such integral charge accumulations should be account for the downshift of the CB and VB positions. Moreover, the more delocalized π–electrons would improve the charge separation efficiency of carbon nitrides.[21a] To support this assumption, the hole- and electron-extraction properties were evaluated by measuring anodic and cathodic photocurrents in the presence of an electron donor (triethanolamine, TEOA), assuming the maximum photocurrent can be obtained without any hole- or electron-transfer limitations.[26] As

shown in Fig. S12, both anodic and cathodic photocurrents at C_5N_2 were less improved than that of g-C_3N_4 by adding TEOA, indicating a superior hole- and electron-extraction property.[25b, 27] Therefore, the theoretical calculations and experimental results collaboratively depicted the critical roles of conjugated linkers in triazine motifs for electronic structure modulation and charge separation efficiency.

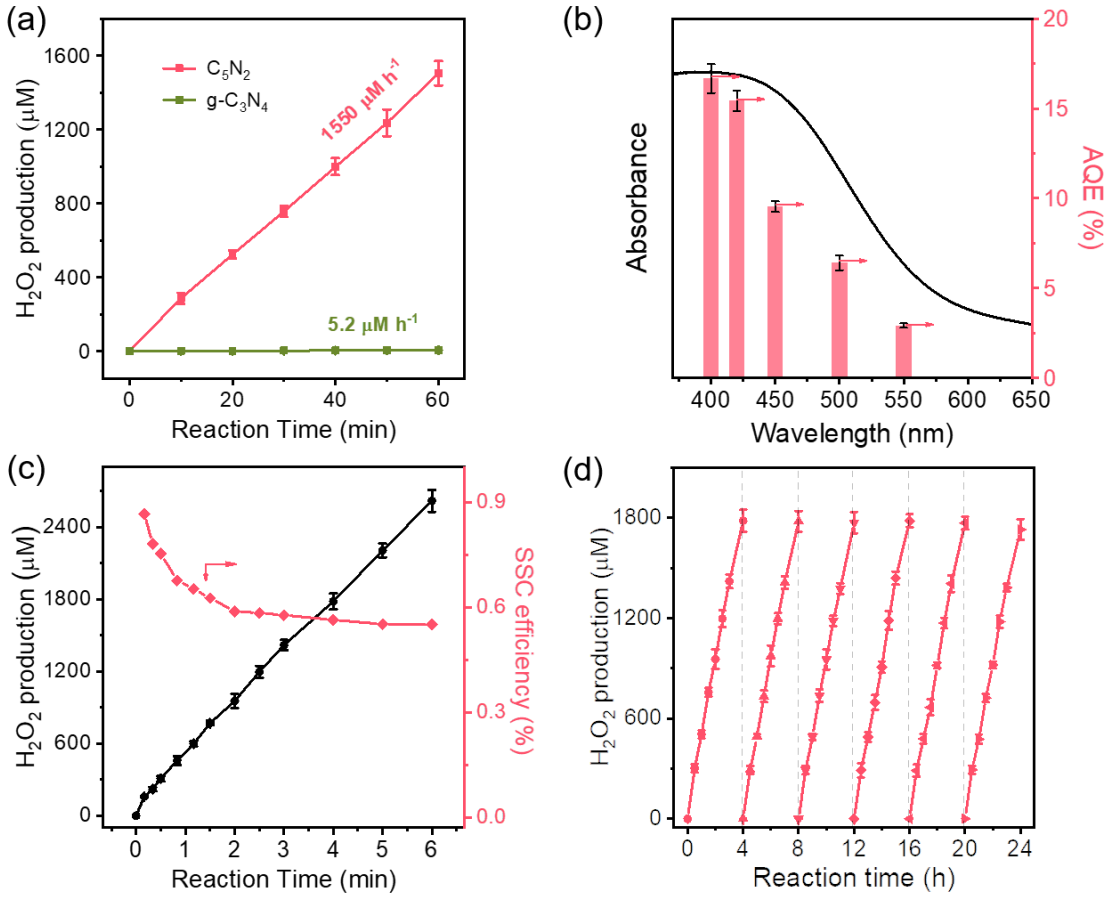

Figure 3. (a) Photocatalytic H_2O_2 production by C_5N_2 or g-C_3N_4 (100 mg) in water (10 mL). (b) Wavelength dependent apparent quantum efficiency (AQE) of C_5N_2 (800 mg) in water (80 mL). (c) Solar-to-chemical conversion (SCC) efficiency of C_5N_2 (1500 mg) in water (150 mL). (d) Stability tests of C_5N_2 (1500 mg) in water (150 mL) for photocatalytic H_2O_2 production. Light source: Xenon lamp, λ> 400 nm, 100 mWcm^{-2}. Error bars represent the standard deviations of three replicate measurements.

In principle, semiconductors with lower CB and VB positions are highly desirable for participating in direct H_2O_2 generation (Eq. 1-3 and Figure 2d). The photocatalytic H_2O_2 production performance of the as-prepared catalysts was evaluated under simulated sunlight irradiation (λ > 400 nm) without any sacrificial agents and co-

catalysts. Fig. 3a and fig. S13 showed the photocatalytic generation H_2O_2 rates of C_5N_2 and g-C_3N_4. The C_5N_2 showed the highest H_2O_2 production rate (1550 μmol L^{-1} per hour), which was about 298 times higher than g-C_3N_4 (5.2 μmol L^{-1} per hour). Fig. 3b and c show the apparent quantum efficiency (AQE) and solar-to-chemical conversion (SCC) efficiency of H_2O_2 production over C_5N_2 in pure water, respectively. The AQE of C_5N_2 at 420 nm was determined to be 15.4% by monochromatic light irradiation, and the SSC efficiency of C_5N_2 reached as high as 0.55% in an oxygenated environment, among the most efficient metal-free photocatalysts for non-sacrificial H_2O_2 production (**Table S3**).[12a, 23h] In addition, the H_2O_2 production rate of C_5N_2 was well maintained after several repeated cycles, suggesting its excellent stability (Fig. 3d).

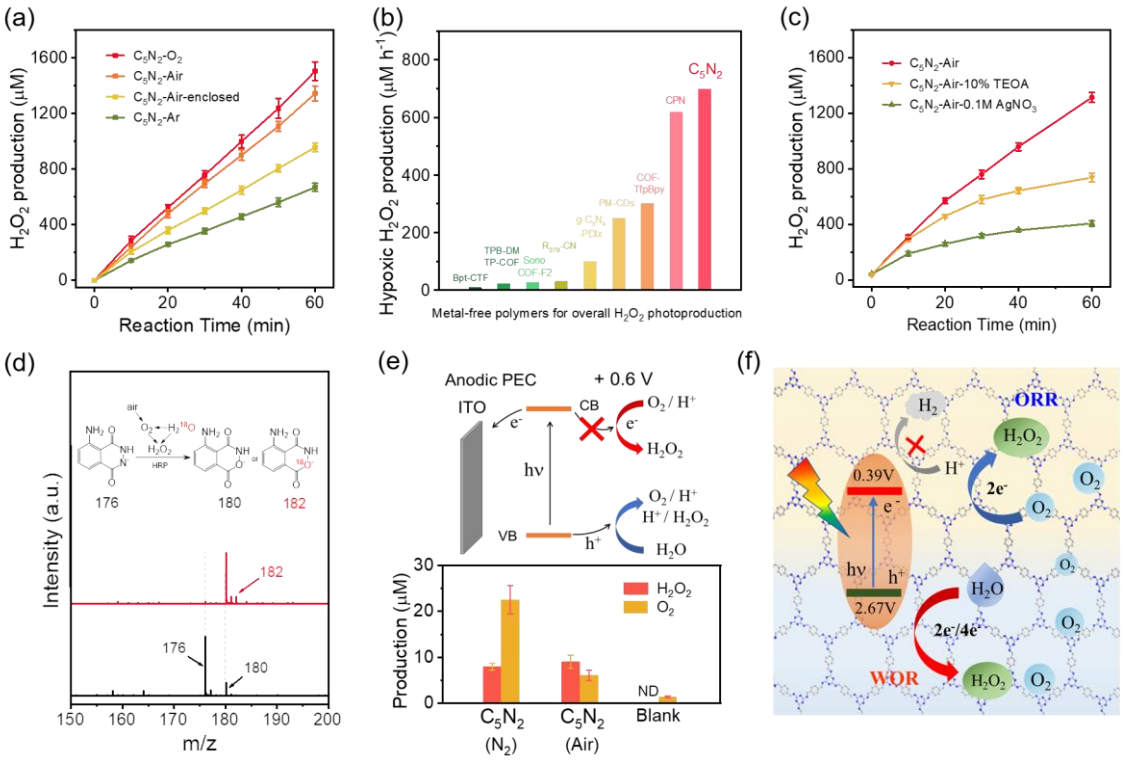

Figure 4. (a) Photocatalytic H_2O_2 production of C_5N_2 with different concentrations of dissolved oxygen. (b) Summary of photocatalytic activity of H_2O_2 production under hypoxic microenvironment by different metal-free polymers in the literature. (c) Photocatalytic H_2O_2 production of C_5N_2 with an electron acceptor ($AgNO_3$, 0.1 M) or an electron donor (TEOA, 10% v/v). Light source: Xenon lamp, λ> 400 nm, 100 mW cm^{-2}. (d) Mass spectra of luminol before (black curve) and after oxidation (red curve) using hydrogen peroxide generated by photocatalytic $H_2{}^{18}O$ splitting in air. (e) Photoelectrochemical production of H_2O_2 and O_2 by C_5N_2 in N_2 and air-saturated electrolyte. Biased potential: 0.6 V vs Ag/AgCl. Inset: the proposed pathway of charge transfer and reactions. (f) Mechanism of photocatalytic H_2O_2 production by C_5N_2.

WOR and ORR were then investigated separately to understand insights into the unusually high efficiency of photocatalytic H_2O_2 production. For this purpose, the aqueous solutions containing different concentrations of dissolved oxygen (Fig. 4a) were explored. It was found that the photocatalytic H_2O_2 production rate was the highest in the O_2-saturated water, while photocatalytic H_2O_2 production rate in Argon (Ar)-saturated solution was still nearly half of that in the O_2-saturated one. Capping the reactor without the supplemental air during the photocatalytic reaction showed a lower reaction rate of H_2O_2 production than in an open-air condition. Strikingly, unlike many previous H_2O_2 photocatalysts,[11a, 23g, 28] the C_5N_2 exhibited a negligible photocatalytic activity for the hydrogen evolution reaction (Fig. S14), owing to the unusual low CB position (> 0 V vs. NHE). These facts suggested that C_5N_2 exhibited a high intrinsic selectivity in O_2 reduction into H_2O_2. Moreover, notably, to our knowledge, C_5N_2 demonstrated the highest H_2O_2 photocatalytic activity under a hypoxic condition among polymeric photocatalysts (Fig. 4b).[2c, d, 12b, 14, 23f, j, 29] It could be explained by that accompanying the exceptionally low CB position, the VB position of C_5N_2 was also relatively low (Fig. 2d), at which, WOR would be more kinetically favorable. In this case, when $2e^-$ ORR was inhibited owing to hypoxic conditions, the pathway of WOR would still work for H_2O_2 production and O_2 production.

Trapping experiments in Fig. 4b showed that not only electron acceptors (e.g., $AgNO_3$) but also electron donors (e.g., TEOA, 10% v/v) made the photocatalytic H_2O_2 production by C_5N_2 decrease, indicating not only ORR but also WOR occurred. Isotope experiments were then performed to verify the existence of $2e^-$ WOR in the first set of experiments. It was supposed that using $H_2{}^{18}O$, $H_2{}^{18}O_2$ would be produced if $2e^-$ photocatalytic WOR occurred. However, $H_2{}^{18}O_2$ was unstable and difficult to be detected by mass spectroscopy. To circumvent this problem, the ^{18}O atom in $H_2{}^{18}O_2$ was transferred into luminol oxide (Fig. 4c inset) by a well-known horseradish peroxidase (HRP)-catalyzed oxidation reaction, accompanying a blue chemiluminescence (Fig. S15).[30] The Liquid chromatography-mass spectra (LC-MS) of the oxidized luminol demonstrated a normal luminol oxide-^{16}O (m/z: 180) peak and a new luminol oxide-^{18}O (m/z: 182) peak, while the control not, confirming the occurrence of the $2e^-$ WOR.

As $4e^-$ WOR is more favorable than $2e^-$ WOR in thermodynamics,[31] the photoelectrochemical (PEC) experiments under normoxic and hypoxic conditions were explored to check whether O_2 was generated via $4e^-$ WOR at the holes or not, using

C_5N_2 modified indium tin oxide (ITO) photoelectrodes. Under anodic photocurrents, the excited electrons in the conduction band were collected by the ITO electrode, and thus the O_2 consumption in the conduction band could be eliminated.[27] As shown in Fig. 4e, the photocatalytic generation of O_2 by C_5N_2 under N_2-saturated electrolyte, was apparent, indicating $4e^-$ WOR existed in the photocatalytic water oxidation by C_5N_2. Under air-saturated electrolyte, it was suppressed to a similar level of H_2O_2 production, presumably ascribed to the chemical equilibrium. In these regards, H_2O_2 was not only produced by a cooperated photocatalytic $2e^-$ ORR and $2e^-$ WOR pathway but also by a synergistic photocatalytic $2e^-$ ORR and $4e^-$ WOR route. In the latter, O_2 generated from $4e^-$ WOR was consumed by the $2e^-$ ORR process to produce H_2O_2 (Fig. 4f).

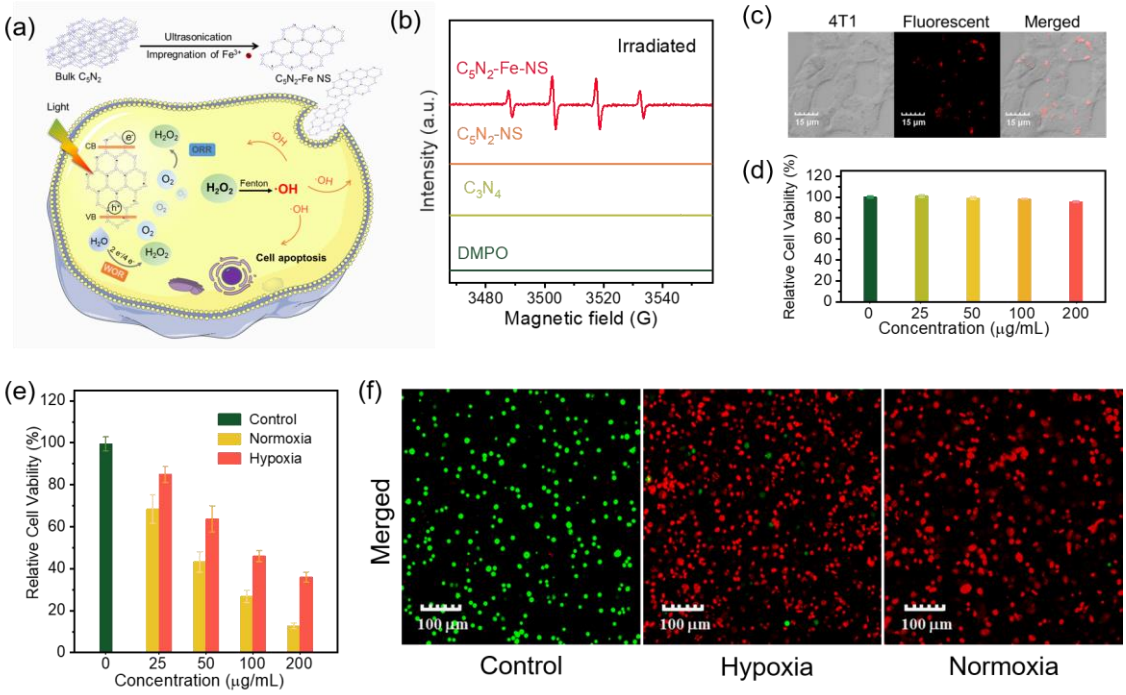

Figure 5. (a) Scheme of therapeutic processes using C_5N_2 through the Fenton reaction generating •OH under light irradiation in hypoxic environments. (b) ESR spectra of C_5N_2-Fe-NS, C_5N_2-NS, g-C_3N_4 powder, DMPO after irradiation. (c) Confocal fluorescence images of 4T1 cells upon incubation with C_5N_2-Fe-NS. Scale bar: 15 μm. (d) Biocompatibility evaluation of C_5N_2-Fe-NS upon incubation with 4T1 cells by WST-8. (e) Cell viability assay of C_5N_2-Fe-NS treated 4T1 cells under light irradiation in hypoxic and normoxic environments. (f) Live/dead double staining of C_5N_2-Fe-NS treated 4T1 cells under light indicated by FDA (green, live cells) and PI (red, dead cells). Scale bar: 100 μm.

In conventional cancer therapy, the PDT utilized light-activated photosensitizers to convert dissolved oxygen (O_2) to attackable ROS,[32] whereas CDT takes advantage of

an *in situ* Fenton or Fenton-like reaction between H_2O_2 and catalysts to generate cytotoxic •OH.[33] However, hypoxia in PDT, insufficient H_2O_2 in CDT, and excess glutathione (GSH) depletion on ROS seriously limit therapy efficiency.[34] As such, many ingenious strategies have been developed to provide the additional intratumoral H_2O_2/O_2 supply, e.g., utilizing poly-mersomes to transport H_2O_2/O_2 into tumor site,[35] applying reactive peroxides (CuO_2, CaO_2 and MgO_2) react with H_2O to improve H_2O_2/O_2 concentration,[36] and *in situ* O_2 production via water splitting by using photocatalysts containing photosensitizer, co-catalysts or heterojunction.[5b, 37] Nonetheless, despite great success in non-sacrificial H_2O_2 production,[ref] metal-free polymeric photocatalysts have been rarely explored for PDT/CDT cancer treatment under hypoxic environment.

As H_2O_2 could not be provided direct potent injury to cancer cells, Fenton reaction are used to produce ·OH via the reaction between Fe^{3+}/Fe^{2+} pair and H_2O_2. For this, the pristine C_5N_2 was exfoliated into nanosheets by ultrasonication and decorated with Fe ions by the traditional impregnation method (C_5N_2-Fe-NS, Fig. S16).[38] We then developed a C_5N_2-based ·OH generator and fluorescence agent for photodynamic hypoxic tumor therapy, which exhibited a competitive tumor inhibition effect (Fig. 5a).

The dynamic light scattering analysis showed the exfoliated C_5N_2-Fe-NS had a hydrodynamic size of 140 nm, and the transmission electron microscopy (TEM) image confirmed the formation of thin nanosheets with small size (Fig. S17).[39] To determine the production of ·OH over different samples, electron spin resonance (ESR) spectroscopies were applied (Fig. 5b and S18). No evident ESR signals for C_5N_2 nanosheets (C_5N_2-NS), g-C_3N_4 powder, 1-pyrroline N-oxide (DMPO), and C_5N_2-Fe-NS in the dark were observed, whereas C_5N_2-Fe-NS exclusively demonstrated typical signals under light irradiation, corresponding to DMPO−·OH adducts. Besides, the production of ·OH was further demonstrated through the Fenton-like reaction using coumarin (cou) as a probe (Fig. S18). The probe displayed a new fluorescence emission enhancement at 455 nm upon the reaction to ·OH. With increased irradiated time, as-produced 7-hydroxy-cou exhibited a gradual amplification of fluorescence intensity with C_5N_2-Fe-NS, indicating that the aptitude of the Fenton-like reaction could be sustainably amplified by light irradiation.[40]

To investigate the accumulation of the C_5N_2-Fe-NS in tumor cells, 4T1 cells were cultured and incubated with C_5N_2-Fe-NS, and the fluorescence confocal imaging was then measured. As shown in Figure 5c, the cytoplasm of the 4T1 cells displayed

prominent fluorescence signals in the red channel, leaving the nucleus with no fluorescence. This observation indicated that C_5N_2-Fe-NS was internalized into the cells with specific localization in the cytoplasm. The *in vitro* cytotoxicity of C_5N_2-Fe-NS was accessed in 4T1 cells by 2-(2-Methoxy-4-nitrophenyl)-3-(4-nitrophenyl)-5-(2,4-disulfophenyl)-2H-tetrazolium Sodium Salt (CCK-8) assay. As shown in Fig. 5d, no noticeable adverse effects were observed in cells after 24 h, indicating the excellent biocompatibility of C_5N_2-Fe-NS. To corroborate the critical role of ROS in the therapeutic effect of C_5N_2-Fe-NS, the contribution of PDT/CDT to total cell death was accessed by carrying out the cell viability (Fig. 5e). Under soft LED light (λ>400nm, 30 mW/ cm^{-2}) for 30 min, C_5N_2-Fe-NS (200 μg/mL) displayed an efficient cell ablation ability (the cell viability of ~12.7%) in a normal microenvironment. Notably, for C_5N_2-Fe-NS in microenvironment containing 1% O_2, the viability of 4T1 cells increased, but was still low (ca. ~35.9%), exhibiting a significant photo-mediated ·OH generation in the hypoxic tumor microenvironment. Meanwhile, fluorescein diacetate (FDA) and propidium iodide (PI) were utilized to stain the live and dead cells, respectively. Live/dead cell staining assay (Fig. 5f) confirmed the comparable significant cell death caused by C_5N_2-Fe-NS in both normoxic and hypoxic cell environments, consistent with the CCK-8 tests. The C_5N_2 with outstanding overall photosynthesis of H_2O_2 exhibited great potential to reverse the hypoxia-triggered therapy resistance with remarkable therapeutic effect. It's worth mentioning that the C_5N_2 could also serve as novel bioimaging agents owing to its superior PL property, and thus provide crucial information for therapy. These results indicate that the C_5N_2 offer an opportunity for building up synchronous imaging and therapy system.

Conclusions

In summary, we report a well-defined metal-free C_5N_2 photocatalyst for selective, efficient, and stable H_2O_2 production without any sacrificial reagents and co-catalysts in both normoxic and hypoxic systems. It was revealed that the strengthened delocalization of π–electrons in C_5N_2 by linkers significantly downshifted the CB/VB position, which facilitated the formation of ideal band position for H_2O_2 production in thermodynamics and kinetics. Accordingly, it intrinsically eliminated the side reaction of HER in photocatalytic H_2O_2 production, promoted the realistic redox selectivity, and endowed an efficient electron-hole separation. As a result, C_5N_2 had an apparent quantum efficiency of 15.4% at 420 nm and a solar-to-chemical conversion efficiency

of 0.55% for H_2O_2 synthesis, among the best overall H_2O_2 production photocatalysts in normoxic systems. More intriguingly, C_5N_2 exhibited the highest efficiency of non-sacrificial photocatalytic H_2O_2 production in hypoxic environments (698 μM/h) so far to our knowledge. Along this line, parallel to industrial H_2O_2 production to address energy and environmental challenges, C_5N_2 was successfully applied to remove hypoxia restriction and further induce conspicuous cancer cell damage in PDT/CDT with synchronous bioimaging. Our findings provided essential insights of linker engineering for idealized electronic structure of carbon nitrides in task specific photocatalytic applications, such as overall H_2O_2 production in this study and presented rising potentials of metal-free carbon nitride not only for sustainable energy and environments but also for emerging PDT/CDT in health.

Reference

[1] a) C. Xia, Y. Xia, P. Zhu, L. Fan, H. Wang, *Science* **2019**, *366*, 226-231; b) S. C. Perry, D. Pangotra, L. Vieira, L.-I. Csepei, V. Sieber, L. Wang, C. Ponce de León, F. C. Walsh, *Nat. Rev. Mater.* **2019**, *3*, 442-458.

[2] a) Y. Shiraishi, T. Takii, T. Hagi, S. Mori, Y. Kofuji, Y. Kitagawa, S. Tanaka, S. Ichikawa, T. Hirai, *Nat. Mater.* **2019**, *18*, 985-993; b) Y. Xia, X. Zhao, C. Xia, Z. Y. Wu, P. Zhu, J. Y. T. Kim, X. Bai, G. Gao, Y. Hu, J. Zhong, Y. Liu, H. Wang, *Nat. Commun.* **2021**, *12*, 4225; c) W. Wang, H. Xie, G. Li, J. Li, P. K. Wong, T. An, *ACS ES&T Water* **2021**, *1*, 1483-1494; d) M. Kou, Y. Wang, Y. Xu, L. Ye, Y. Huang, B. Jia, H. Li, J. Ren, Y. Deng, J. Chen, Y. Zhou, K. Lei, L. Wang, W. Liu, H. Huang, T. Ma, *Angew. Chem. Int. Ed.* **2022**, *61*, 1521-3773.

[3] a) M. Dewaele, H. Maes, P. Agostinis, *Autophagy* **2014**, *6*, 838-854; b) Q. Chen, C. Liang, X. Sun, J. Chen, Z. Yang, H. Zhao, L. Feng, Z. Liu, *Proc. Natl. Acad. Sci. USA* **2017**, *114*, 5343-5348.

[4] a) J. Kim, H. R. Cho, H. Jeon, D. Kim, C. Song, N. Lee, S. H. Choi, T. Hyeon, *J. Am. Chem. Soc.* **2017**, *139*, 10992-10995; b) X. Li, N. Kwon, T. Guo, Z. Liu, J. Yoon, *Angew. Chem. Int. Ed.* **2018**, *57*, 11522-11531; c) S. Z. F. Phua, G. Yang, W. Q. Lim, A. Verma, H. Chen, T. Thanabalu, Y. Zhao, *ACS Nano* **2019**, *13*, 4742-4751; d) Y. Wan, L. H. Fu, C. Li, J. Lin, P. Huang, *Adv. Mater.* **2021**, *33*, e2103978.

[5] a) Z. Tang, Y. Liu, M. He, W. Bu, *Angew. Chem. Int. Ed.* **2019**, *58*, 946-956; b) Y. Li, R. Jia, H. M. Lin, X. L. Sun, F. Y. Qu, *Adv. Funct. Mater.* **2021**, *31*, e2008420; c) Y. Sang, F. Cao, W. Li, L. Zhang, Y. You, Q. Deng, K. Dong, J. Ren, X. Qu, *J. Am. Chem. Soc.* **2020**, *142*, 5177-5183; d) L. H. Fu, Y. Wan, C. Qi, J. He, C. Li, C. Yang, H. Xu, J. Lin, P. Huang, *Adv. Mater.* **2021**, *33*, e2006892; e) S. L. Li, P. Jiang, F. L. Jiang, Y. Liu, *Adv. Funct. Mater.* **2021**, *31*, e2100243.

[6] Y. Wang, G. I. N. Waterhouse, L. Shang, T. Zhang, *Adv. Energy Mater.* **2020**, *11*, e1802525.

[7] a) Y. Sun, L. Han, P. Strasser, *Chem. Soc. Rev.* **2020**, *49*, 6605-6631; b) H. Hou, X. Zeng, X. Zhang, *Angew. Chem. Int. Ed.* **2020**, *59*, 17356-17376.

[8] H. Cheng, J. Cheng, L. Wang, H. Xu, *Chem. Mater.* **2022**, *34*, 4259-4273.

[9] a) C. Chu, Q. Zhu, Z. Pan, S. Gupta, D. Huang, Y. Du, S. Weon, Y. Wu, C. Muhich, E. Stavitski, K. Domen, J. H. Kim, *Proc. Natl. Acad. Sci. USA* **2020**, *117*, 6376-6382; b) T. Liu, Z. Pan, J. J. M. Vequizo, K. Kato, B. Wu, A. Yamakata, K. Katayama, B. Chen, C. Chu, K. Domen, *Nat. Commun.* **2022**, *13*, 1034.

[10] a) Y. Kofuji, Y. Isobe, Y. Shiraishi, H. Sakamoto, S. Tanaka, S. Ichikawa, T. Hirai, *J. Am. Chem. Soc.* **2016**, *138*, 10019-10025; b) L. Chen, L. Wang, Y. Wan, Y. Zhang, Z. Qi, X. Wu, H. Xu, *Adv. Mater.* **2020**, *32*, e1904433.

[11] a) H. Cheng, H. Lv, J. Cheng, L. Wang, X. Wu, H. Xu, *Adv. Mater.* **2022**, *34*, e2107480; b) X. Zhang, P. Ma, C. Wang, L. Gan, X. Chen, P. Zhang, Y. Wang, H. Li, L. Wang, X. Zhou, K. Zheng, *Energy Environ. Sci.* **2022**, *15*, 830-842.

[12] a) Z. Teng, Q. Zhang, H. Yang, K. Kato, W. Yang, Y.-R. Lu, S. Liu, C. Wang, A. Yamakata, C. Su, B. Liu, T. Ohno, *Nat. Catal.* **2021**, *4*, 374-384; b) J. J. Cao, H. Wang, Y. J. Zhao, Y. Liu, Q. Y. Wu, H. Huang, M. W. Shao, Y. Liu, Z. H. Kang, *J. Mater. Chem. A* **2020**, *8*, 3701-3707.

[13] a) Y. Kofuji, S. Ohkita, Y. Shiraishi, H. Sakamoto, S. Tanaka, S. Ichikawa, T. Hirai, *ACS Catal.* **2016**, *6*, 7021-7029; b) Y. Kofuji, S. Ohkita, Y. Shiraishi, H. Sakamoto, S. Ichikawa, S. Tanaka,

T. Hirai, *ACS Sustain. Chem. Eng.* **2017**, *5*, 6478-6485.

[14] C. Wu, Z. Teng, C. Yang, F. Chen, H. B. Yang, L. Wang, H. Xu, B. Liu, G. Zheng, Q. Han, *Adv. Mater.* **2022**, *34*, e2110266.

[15] W. Dai, F. Shao, J. Szczerbiński, R. McCaffrey, R. Zenobi, Y. Jin, A. D. Schlüter, W. Zhang, *Angew. Chem. Int. Ed.* **2016**, *128*, 221-225.

[16] M. Matsumoto, R. R. Dasari, W. Ji, C. H. Feriante, T. C. Parker, S. R. Marder, W. R. Dichtel, *J. Am. Chem. Soc.* **2017**, *139*, 4999-5002.

[17] X. B. Huang, Z. Y. Wu, H. Y. Zheng, W. J. Dong, G. Wang, *Green Chem.* **2018**, *20*, 664-670.

[18] J. Xie, S. A. Shevlin, Q. Ruan, S. J. A. Moniz, Y. Liu, X. Liu, Y. Li, C. C. Lau, Z. X. Guo, J. Tang, *Energy Environ. Sci.* **2018**, *11*, 1617-1624.

[19] S. Bi, C. Yang, W. Zhang, J. Xu, L. Liu, D. Wu, X. Wang, Y. Han, Q. Liang, F. Zhang, *Nat. Commun.* **2019**, *10*, 2467.

[20] a) Z. Zhou, J. Wang, J. Yu, Y. Shen, Y. Li, A. Liu, S. Liu, Y. Zhang, *J. Am. Chem. Soc.* **2015**, *137*, 2179-2182; b) C. Huang, J. Wen, Y. Shen, F. He, L. Mi, Z. Gan, J. Ma, S. Liu, H. Ma, Y. Zhang, *Chem Sci.* **2018**, *9*, 7912-7915.

[21] a) P. Kumar, E. Vahidzadeh, U. K. Thakur, P. Kar, K. M. Alam, A. Goswami, N. Mahdi, K. Cui, G. M. Bernard, V. K. Michaelis, K. Shankar, *J. Am. Chem. Soc.* **2019**, *141*, 5415-5436; b) I. Y. Kim, S. Kim, S. Premkumar, J. H. Yang, S. Umapathy, A. Vinu, *Small* **2019**, *16*, e1903572.

[22] H. Yang, Q. Zhou, Z. Fang, W. Li, Y. Zheng, J. Ma, Z. Wang, L. Zhao, S. Liu, Y. Shen, Y. Zhang, *Chem* **2021**, *7*, 2708-2721.

[23] a) Y. Shiraishi, S. Kanazawa, Y. Kofuji, H. Sakamoto, S. Ichikawa, S. Tanaka, T. Hirai, *Angew. Chem. Int. Ed.* **2014**, *53*, 13454-13459; b) H. Ou, P. Yang, L. Lin, M. Anpo, X. Wang, *Angew. Chem. Int. Ed.* **2017**, *56*, 10905-10910; c) Y. Kofuji, Y. Isobe, Y. Shiraishi, H. Sakamoto, S. Ichikawa, S. Tanaka, T. Hirai, *ChemCatChem* **2018**, *10*, 2070-2077; d) Y. Shiraishi, T. Hagi, M. Matsumoto, S. Tanaka, S. Ichikawa, T. Hirai, *Commun. Chem.* **2020**, *3*, 169; e) Z. Teng, W. Cai, S. Liu, C. Wang, Q. Zhang, S. Chenliang, T. Ohno, *Appl. Catal. B Environ.* **2020**, *271*, 118917; f) L. Li, L. Xu, Z. Hu, J. C. Yu, *Adv. Funct. Mater.* **2021**, *31*, 1616-3028; g) L. Liu, M.-Y. Gao, H. Yang, X. Wang, X. Li, A. I. Cooper, *J. Am. Chem. Soc.* **2021**, *143*, 19287-19293; h) Y. Shiraishi, M. Matsumoto, S. Ichikawa, S. Tanaka, T. Hirai, *J. Am. Chem. Soc.* **2021**, *143*, 12590-12599; i) Q. Tian, L. Jing, S. Ye, J. Liu, R. Chen, C. A. H. Price, F. Fan, J. Liu, *Small* **2021**, *17*, e2103224; j) Q. Wu, J. Cao, X. Wang, Y. Liu, Y. Zhao, H. Wang, Y. Liu, H. Huang, F. Liao, M. Shao, Z. Kang, *Nat. Commun.* **2021**, *12*, 483; k) Y.-X. Ye, J. Pan, Y. Shen, M. Shen, H. Yan, J. He, X. Yang, F. Zhu, J. Xu, J. He, G. Ouyang, *Proc. Natl. Acad. Sci. USA* **2021**, *118*; l) H. Wang, C. Yang, F. Chen, G. Zheng, Q. Han, *Angew. Chem. Int. Ed.* **2022**, *61*, e202202328; m) W. Zhao, P. Yan, B. Li, M. Bahri, L. Liu, X. Zhou, R. Clowes, N. D. Browning, Y. Wu, J. W. Ward, A. I. Cooper, *J. Am. Chem. Soc.* **2022**, *144*, 9902-9909.

[24] H. Schlomberg, J. Kröger, G. Savasci, M. W. Terban, S. Bette, I. Moudrakovski, V. Duppel, F. Podjaski, R. Siegel, J. Senker, R. E. Dinnebier, C. Ochsenfeld, B. V. Lotsch, *Chem. Mater.* **2019**, *31*, 7478-7486.

[25] a) Y. Zhang, M. Antonietti, *Chem Asian J* **2010**, *5*, 1307-1311; b) C. Huang, Y. Wen, J. Ma, D. Dong, Y. Shen, S. Liu, H. Ma, Y. Zhang, *Nat. Commun.* **2021**, *12*, 320.

[26] G. Peng, J. Albero, H. Garcia, M. Shalom, *Angew. Chem. Int. Ed.* **2018**, *57*, 15807-15811.

[27] T. Zhao, Q. Zhou, Y. Lv, D. Han, K. Wu, L. Zhao, Y. Shen, S. Liu, Y. Zhang, *Angew. Chem. Int. Ed.* **2019**, *59*, 1139-1143.

[28] Y. Fu, C. a. Liu, M. Zhang, C. Zhu, H. Li, H. Wang, Y. Song, H. Huang, Y. Liu, Z. Kang, *Adv. Energy Mater.* **2018**, *8*, e1802525.

[29] a) W. Zhao, P. Yan, B. Li, M. Bahri, L. Liu, X. Zhou, R. Clowes, N. D. Browning, Y. Wu, J. W. Ward, A. I. Cooper, *J. Am. Chem. Soc.* **2022**, *144*, 9902-9909; b) Z. Zhu, H. Pan, M. Murugananthan, J. Gong, Y. Zhang, *Appl. Catal. B Environ.* **2018**, *232*, 19-25.

[30] X. Li, Y. Du, H. Wang, H. Ma, D. Wu, X. Ren, Q. Wei, J.-J. Xu, *Anal. Chem.* **2020**, *92*, 12693-12699.

[31] K. Fuku, K. Sayama, *Chem. Commun.* **2016**, *52*, 5406-5409.

[32] a) J.-n. Liu, W. Bu, J. Shi, *Chem. Rev.* **2017**, *117*, 6160-6224; b) X. Zhao, J. Liu, J. Fan, H. Chao, X. Peng, *Chem. Soc. Rev.* **2021**, *50*, 4185-4219.

[33] a) C. Cao, X. Wang, N. Yang, X. Song, X. Dong, *Chem Sci.* **2022**, *13*, 863-889; b) C. Jia, Y. Guo, F. G. Wu, *Small* **2021**, *18*, e2103868.

[34] C. Liu, Y. Cao, Y. Cheng, D. Wang, T. Xu, L. Su, X. Zhang, H. Dong, *Nat. Commun.* **2020**, *11*, 1735.

[35] a) W.-P. Li, C.-H. Su, Y.-C. Chang, Y.-J. Lin, C.-S. Yeh, *ACS Nano* **2016**, *10*, 2017-2027; b) X. Song, J. Xu, C. Liang, Y. Chao, Q. Jin, C. Wang, M. Chen, Z. Liu, *Nano Lett.* **2018**, *18*, 6360-6368.

[36] a) S. Zhang, C. Cao, X. Lv, H. Dai, Z. Zhong, C. Liang, W. Wang, W. Huang, X. Song, X. Dong, *Chem Sci.* **2020**, *11*, 1926-1934; b) J. Shen, H. Yu, Y. Shu, M. Ma, H. Chen, *Adv. Funct. Mater.* **2021**, *31*, e2106106; c) H. Hu, L. Yu, X. Qian, Y. Chen, B. Chen, Y. Li, *Adv. Sci.* **2020**, *8*, e2000494.

[37] a) D.-W. Zheng, B. Li, C.-X. Li, J.-X. Fan, Q. Lei, C. Li, Z. Xu, X.-Z. Zhang, *ACS Nano* **2016**, *10*, 8715-8722; b) Z. Chen, A. Savateev, S. Pronkin, V. Papaefthimiou, C. Wolff, M. G. Willinger, E. Willinger, D. Neher, M. Antonietti, D. Dontsova, *Adv. Mater.* **2017**, *29*, e28632318; c) Y. Cheng, X. Kong, Y. Chang, Y. Feng, R. Zheng, X. Wu, K. Xu, X. Gao, H. Zhang, *Adv. Mater.* **2020**, *32*, e1908109.

[38] a) Y. Li, S. Ouyang, H. Xu, X. Wang, Y. Bi, Y. Zhang, J. Ye, *J. Am. Chem. Soc.* **2016**, *138*, 13289-13297; b) X. Zhang, X. Xie, H. Wang, J. Zhang, B. Pan, Y. Xie, *J. Am. Chem. Soc.* **2012**, *135*, 18-21.

[39] Z. Zhou, Q. Shang, Y. Shen, L. Zhang, Y. Zhang, Y. Lv, Y. Li, S. Liu, Y. Zhang, *Anal. Chem.* **2016**, *88*, 6004-6010.

[40] P. Li, J. Li, X. Feng, J. Li, Y. Hao, J. Zhang, H. Wang, A. Yin, J. Zhou, X. Ma, B. Wang, *Nat. Commun.* **2019**, *10*, 2177.